

Smooth Tensor Qatar Riyal Decomposition for Dynamic MRI Reconstruction

Tingting Xu, Yongyong Chen, *Member, IEEE*, Haijin Zeng, Guokai Zhang, and Jingyong Su

Abstract—Dynamic magnetic resonance imaging (dMRI) speed and imaging quality have always been a crucial issue in medical imaging research. Most existing methods characterize the tensor rank-based minimization to reconstruct dMRI from sampling k - t space data. However, (1) these approaches that unfold the tensor along each dimension destroy the inherent structure of dMR images. (2) they focus on preserving global information only, while ignoring the local details reconstruction such as the spatial piece-wise smoothness and sharp boundaries. To overcome these obstacles, we suggest a novel low-rank tensor decomposition approach by integrating tensor Qatar Riyal (QR) decomposition, low-rank tensor nuclear norm, and asymmetric total variation to reconstruct dMRI, named TQRTV. Specifically, while preserving the tensor inherent structure by utilizing tensor nuclear norm minimization to approximate tensor rank, QR decomposition reduces the dimensions in the low-rank constraint term, thereby improving the reconstruction performance. TQRTV further exploits the asymmetric total variation regularizer to capture local details. Numerical experiments demonstrate that the proposed reconstruction approach is superior to the existing ones.

Index Terms—Dynamic MRI reconstruction, tensor Qatar Riyal decomposition, tensor total variation.

I. INTRODUCTION

DYNAMIC magnetic resonance imaging (dMRI) with plentiful spatial and temporal information, as an important imaging technique, can dynamically monitor the physiological phenomena of the human body over time and depict the image of the internal structure, which has been widely used in many clinical applications, including computer-aided diagnosis [1], [2], PET attenuation correction [3] and age estimation [4]. However, the imaging speed of dMRI and the imaging

This work was supported in part by the National Natural Science Foundation of China under Grant 62106063, by the Guangdong Natural Science Foundation under Grants 2022A1515010819 and 2022A1515010800, by the Shenzhen College Stability Support Plan under Grant GXWD20201230155427003-20200824113231001, by the Shenzhen Science and Technology Program under Grants RCBS20210609103708013 and JCYJ20220818102414031, by Humanities and Social Sciences Foundation of the Ministry of Education of China under Grant 22YJC630129, and by Guangdong Provincial Key Laboratory of Novel Security Intelligence Technologies under Grant 2022B1212010005. (Corresponding author: Yongyong Chen).

T. Xu, Y. Chen and J. Su are with School of Computer Science and Technology, Harbin Institute of Technology, Shenzhen 518055, China. Y. Chen is also with Guangdong Provincial Key Laboratory of Novel Security Intelligence Technologies (Email: YongyongChen.cn@gmail.com).

H. Zeng is with Image Processing and Interpretation, imec research group at Ghent University, Belgium (Email: Haijin.Zeng@UGent.be).

G. Zhang is with School of Optical-Electrical and Computer Engineering, University of Shanghai for Science and Technology, Shanghai 10001, China (Email: zhangguokai.01@163.com).

quality are two determining factors to attribute to its potential and application value. Slow imaging speed costs much long time to obtain a high-resolution image, facing serious health risks for patients, and some motion and aliasing artifacts are inevitably introduced [5], thereby limiting its applicability range. Therefore, how to improve the imaging speed of dMRI with quality guarantee is a crucial and concerned issue in the medical imaging research.

To accelerate the acquisition of dMRI, many approaches have been proposed in recent years. Due to the attractive reconstruction performance, compressed sensing (CS) has received considerable attention by exploring sparse representation of dMR images in the transform domains [6] including the Fourier domain and Karhunen Louve transform domain [7]. Moreover, taking advantage of high spatio-temporal correlation of dynamic images, researchers have also exploited the low-rank nature of matrices by reshaping each time frame as a column of the reconstructed matrix and the number of extracted time frames determines the size of the matrix [8]–[10]. A few large singular values in the transformed matrix are utilized to preserve the main information of the reconstructed matrix [7], [11]. Since there exists good complementarity among different priors, sparsity and total variation are also frequently combined with low-rank regularizer to reconstruct dynamic images [12]–[17].

Robust principal component analysis (RPCA) model, which divides the given matrix into the low-rank part L and sparse part S [18], has been applied to reconstruct dMRI [19]–[22]. The cross-section of the dMRI data and its low-rank part and sparse part are further drawn in Fig. 1. As we observed, the component L changes slowly along the time dimension, which can be modeled by the low-rank nature [23], [24]. The distribution of S is scattered, thus it can be well constructed by sparse feature. Based on this, Gao *et al.* [25], [26], Otazo *et al.* [22], and Trémouh  ac *et al.* [27] followed the general idea of RPCA for dMRI reconstruction. Lin *et al.* [28] further extended RPCA for Dynamic Parallel MRI Reconstruction. However, dMRI data, as high-dimensional tensor data, contains information in both temporal and spatial dimensions. The RPCA model rearranges the tensor data into one matrix by the unfolding operator, which would destroy the intrinsic structural information and cannot fully explore the low rankness of original data.

To alleviate the above issue, tensor decomposition-based approaches have been put forward to keep multi-dimensional data structure instead of simply unfolding [29], [30]. For example, dMRI data are represented as one low-rank tensor

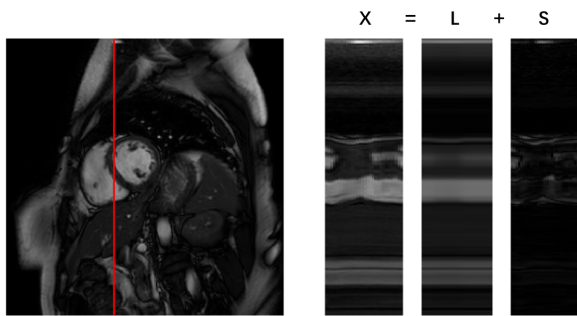


Fig. 1: The red line in the left figure is the cross-section position on the cardiac cine dataset. The right figure shows the low-rank part and sparse part of the cross-section.

for reconstruction in [31]. Besides, the authors in [32] utilized the tensor version of RPCA (TRPCA) to preserve the internal structure information of the data by using multidimensional tensor trace norm dMRI recovery. In TRPCA, the dMRI data is decomposed into low-rank and sparse parts ($\mathcal{L} + \mathcal{S}$). Considering the block-wise smoothness of tensor data, Liu *et al.* [33] proposed a smooth TRPCA model. Subsequently, the weighted tensor nuclear norm was utilized to impose the low-rank nature in \mathcal{L} [34]. However, the low-rank nature in [34] is based on the unfolding operation to define the tensor nuclear norm of three unfolding matrices, which still leads to the loss of spatio-temporal structural information to some extent. Recently, tensor singular value decomposition (t-SVD) [35] has been proposed for the low-rank tensor recovery problem. After that, as an expansion of the matrix completion method [36], an approximate t-SVD method based on tensor Qatar Riyal (T-QR) decomposition for third-order tensor was proposed [37]. Wu *et al.* further utilized the method in [37] and the tensor nuclear norm (TNN) to achieve a better algorithm for tensor completion [38]. Ai *et al.* introduced the t-SVD to dynamic MRI reconstruction by combining the convex relaxation of t-SVD, the TNN, and the l_1 norm of tensor gradient [39]. Zhang *et al.* proposed to combine the TNN and Casorati matrix nuclear norm regularizers to reconstruct dMRI [40]. It is worth noting that with the vigorous development of artificial intelligence, more and more researchers have applied deep learning theory to various fields and made remarkable achievements [41]–[44]. The studies in [42], [43] are seminal works by applying deep learning theory to dynamic MRI reconstruction. Subsequently, dynamic MRI reconstruction algorithms based on convolutional neural networks have been continuously improved [45]–[47].

In this paper, we put forward a novel low-rank tensor decomposition approach named TQRTV by integrating the T-QR decomposition, the TNN, and asymmetric total variation for dMRI reconstruction. Compared with SVD, QR decomposition is faster to acquire singular values and vectors [38]. Therefore, by utilizing T-QR decomposition, we obtain the r biggest singular values in each frontal slice of the Fourier transformed data, and thereby carrying out the low-rank tensor property. After that, we enforce the TNN constraint

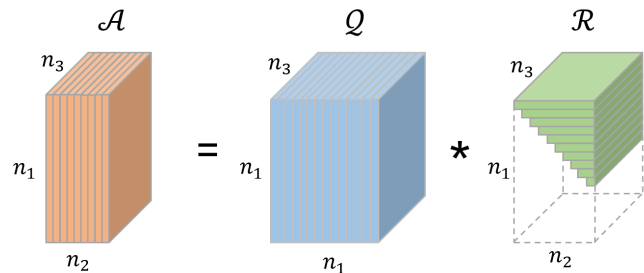


Fig. 2: The tensor QR decomposition.

on the resulting lower triangular tensor with small dimension to enhance reconstruction efficiency and performance. Meanwhile, the asymmetric three dimensional total variation (TV) regularizer term is also exploited to capture local details and reconstruct edges and boundaries. The well-known alternating direction method of multipliers (ADMM) is adopted to tackle the TQRTV model. We conduct experiments on the phantom, cardiac cine, and cardiac perfusion datasets to verify the advantages of our method compared to existing methods.

The remaining parts of this article are arranged as follows. In Section II, we introduce several preliminaries applied throughout this article. Section III gives our dMRI reconstruction model TQRTV and the optimization algorithm based on ADMM. In Section IV, we conduct correlative experiments to evaluate the effectiveness of the proposed TQRTV. Finally, this paper is concluded in Section V.

II. BACKGROUND

A. Notations and Preliminaries

In this paper, we use notations a , \mathbf{a} , A , \mathcal{A} to denote scalar, vector, matrix, and tensor, respectively. I and \mathcal{I} denote identity matrix and identity tensor, respectively. We use $Tr(\cdot)$ to express the trace of matrix. The superscript T and -1 are the transpose and inversion operators, respectively. \mathcal{A}_{ijk} denotes the (i, j, k) -th entry of tensor \mathcal{A} . $\mathcal{A}(:, :, k)$ or $\mathcal{A}^{(k)}$ is the k -th frontal slice of tensor \mathcal{A} . The unfolding operator is used to transform tensor $\mathcal{A} \in \mathbb{R}^{n_1 \times n_2 \times n_3}$ into a matrix $A^{(k)} \in \mathbb{R}^{n_k \times (\prod_{i=1, i \neq k}^d n_i)}$, and the folding operator is the inverse operation of unfolding. Besides, $\bar{\mathcal{A}} = \text{fft}(\mathcal{A}, [], 3)$ represents the discrete Fourier transform (DFT) of tensor \mathcal{A} along the third dimension. The corresponding inverse discrete Fourier transform is denoted as $\mathcal{A} = \text{ifft}(\bar{\mathcal{A}}, [], 3)$. $\langle \mathcal{A}, \mathcal{B} \rangle = \sum_{ijk} a_{ijk} b_{ijk}$ denotes the inner product of two tensors. $\|\mathcal{A}\|_F = \sqrt{\langle \mathcal{A}, \mathcal{A} \rangle} = \sqrt{\sum_{ijk} \mathcal{A}_{ijk}^2}$ represents the Frobenius norm of \mathcal{A} .

Definition 1: (t-Product [48]): Given the tensors $\mathcal{A} \in \mathbb{R}^{n_1 \times n_2 \times n_3}$, and $\mathcal{B} \in \mathbb{R}^{n_2 \times n_4 \times n_3}$, we can get the tensor-tensor-product (t-product) as follows:

$$\mathcal{C}(i, j, :) = \sum_{m=1}^{n_2} \mathcal{A}(i, m, :) * \mathcal{B}(m, j, :),$$

where $*$ indicates the circular convolution.

Definition 2: (Special Tensors [48]): The conjugate transpose of $\mathcal{A} \in \mathbb{R}^{n_1 \times n_2 \times n_3}$ is defined as $\mathcal{A}^T \in \mathbb{R}^{n_2 \times n_1 \times n_3}$,

whose frontal slices is conjugate transposed and the order of the second to n_3 -th frontal slices is reversed. $\mathcal{I} \in \mathbb{R}^{n_1 \times n_1 \times n_3}$ denotes the identity tensor whose $\mathcal{I}^{(1)} \in \mathbb{R}^{n_1 \times n_1}$ is an identity matrix and the rest are zero. $\mathcal{Q} \in \mathbb{R}^{n_1 \times n_1 \times n_3}$ is an orthogonal tensor as long as it satisfies $\mathcal{Q}^T * \mathcal{Q} = \mathcal{Q} * \mathcal{Q}^T = \mathcal{I}$.

Definition 3: (Low Triangular Tensor): Let $\mathcal{A} \in \mathbb{R}^{n_1 \times n_2 \times n_3}$ denotes a lower triangular tensor whose each frontal slice is a lower triangular matrix.

Definition 4: (t-SVD [49]): Given a tensor $\mathcal{A} \in \mathbb{R}^{n_1 \times n_2 \times n_3}$, its tensor singular values decomposition is written as follows

$$\mathcal{A} = \mathcal{U} * \mathcal{S} * \mathcal{V}^T,$$

where $\mathcal{U} \in \mathbb{R}^{n_1 \times n_1 \times n_3}$ and $\mathcal{V} \in \mathbb{R}^{n_2 \times n_2 \times n_3}$ denote orthogonal tensor, and $\mathcal{S} \in \mathbb{R}^{n_1 \times n_2 \times n_3}$ denotes an f-diagonal tensor each of whose frontal slices is a diagonal matrix.

Definition 5: (Tensor Tubal Rank [48]): For a third-order tensor, its tensor tubal rank is defined as the number of nonzero singular tubes of \mathcal{S} , where \mathcal{S} is gained by t-SVD.

Definition 6: (Tensor Nuclear Norm [48]): The tensor nuclear norm of $\mathcal{A} \in \mathbb{R}^{n_1 \times n_2 \times n_3}$ is written as follows:

$$\|\mathcal{A}\|_* = \sum_{i=1}^{n_3} \|\bar{\mathcal{A}}^{(i)}\|_*, \quad (1)$$

where $\|\bar{\mathcal{A}}^{(i)}\|_*$ denotes the nuclear norm of the matrix $\bar{\mathcal{A}}^{(i)}$.

Definition 7: (Tensor Qatar Riyal Decomposition [48]): Given a tensor $\mathcal{A} \in \mathbb{R}^{n_1 \times n_2 \times n_3}$, its tensor Qatar Riyal decomposition is formulated as

$$\mathcal{A} = \mathcal{Q} * \mathcal{R},$$

where \mathcal{Q} denotes an orthogonal tensor of size $n_1 \times n_1 \times n_3$, and \mathcal{R} is analogous to the upper triangular tensor of size $n_1 \times n_2 \times n_3$. An illustration of the tensor QR decomposition is shown in Fig. 2.

B. QR Decomposition-based Methods

For the matrix recovery problem, Liu *et al.* proposed a QR decomposition based fast tri-factorization (FTF) approach [50]. Specifically, for a real matrix A of size $n_1 \times n_2$ and rank r ($r \in [1, \min\{n_1, n_2\}]$), its tri-factorization can be formulated as

$$A = LDR, \quad (2)$$

where L and R are the orthogonal matrices with the dimension of $n_1 \times r$ and $r \times n_2$, respectively. D is a lower triangular matrix of size $r \times r$. After that, considering this tri-factorization decomposition approach, [36], developed a new method based on QR decomposition for calculating the approximate SVD of a matrix and the optimization problem is formulated as

$$\begin{aligned} \min_{L,D,R} \alpha \|D\|_{2,1} + \frac{1}{2} \|LDR - Y\|_F^2 \\ \text{s.t. } X = LDR, \end{aligned} \quad (3)$$

where $\|D\|_{2,1} = \sum_{i=1}^r \sqrt{\sum_{j=1}^r |D_{i,j}|^2}$ represents the $L_{2,1}$ -norm of a matrix, $\alpha > 0$, and Y is the given matrix. Subsequently, Zheng *et al.* extended model (3) into the tensor recovery problem and proposed a novel CTSVD-QR method to compute an approximate t-SVD based on tensor $L_{2,1}$ -norm

and tensor QR decomposition (T-QR) [37]. The calculation details of CTSVD-QR are placed in the appendix. The corresponding tensor recovery model is written as follows:

$$\begin{aligned} \min_{\mathcal{D}} \|\mathcal{D}\|_{2,1} \\ \text{s.t. } \begin{cases} \mathcal{X} = \mathcal{L} * \mathcal{D} * \mathcal{R} \\ \mathcal{P}_{\Omega}(\mathcal{X}) = \mathcal{P}_{\Omega}(\mathcal{A}) \end{cases}, \end{aligned} \quad (4)$$

where $\mathcal{L} \in \mathbb{R}^{n_1 \times r \times n_3}$ and $\mathcal{R} \in \mathbb{R}^{r \times n_2 \times n_3}$ are the orthogonal tensors, and $\mathcal{D} \in \mathbb{R}^{r \times r \times n_3}$ ($r \in [1, \min\{n_1, n_2\}]$) is a lower triangular tensor. $\mathcal{P}_{\Omega}(\cdot)$ denotes the projection operator which holds the elements in Ω consistent, while the rest be zeros.

C. Problem Formulation

The acquisition equation of dynamic MRI in the \mathbf{k} - t space could be written as

$$b_{k,t} = \int_r x_{r,t} e^{(-2j\pi k \cdot r)} dr + e_{k,t}, \quad (5)$$

where $b_{k,t}$ indicates the metrical \mathbf{k} - t space signal, $x_{r,t}$ represents the recovered image series, and $e_{k,t}$ denotes the noise with an additive white Gaussian distribution [51].

For multidimensional signals like dMRI with n_3 frames, we can utilize the Tucker product as the way to build the sparsity bases and measurement matrices [32], [52]. With this framework, assuming \mathcal{X} be n_3 frame images of dimension $n_1 \times n_2$, and $\mathcal{Y} \in \mathbb{R}^{m_1 \times m_2 \times m_3}$, the tensor form of Eq. (5) can be indicated in discrete form as follows:

$$\mathcal{Y} = \mathcal{X} \times_1 \Phi_1 \times_2 \Phi_2 \times_3 \Phi_3 + \mathcal{E} = \mathbb{T}(\mathcal{X}) + \mathcal{E}, \quad (6)$$

where Φ_1 with size $n_1 \times m_1$ and Φ_2 with size $n_2 \times m_2$ are under-sampled \mathbf{k} space encoders, and $m_1 \leq n_1$, $m_2 \leq n_2$, while Φ_3 with size $n_3 \times n_3$ expresses the identity matrix. \mathcal{E} denotes the noise, and we use \mathbb{T} operator, defined as $\mathbb{T}(\mathcal{X}) = \mathcal{X} \times_1 \Phi_1 \times_2 \Phi_2 \times_3 \Phi_3$, to represent this under-sampled process.

III. OUR METHOD

We will first introduce the proposed dMRI reconstruction model based on T-QR decomposition and asymmetric total variation. Then, an ADMM-based optimization algorithm is proposed to tackle the proposed model.

A. The Proposed Model

Among the previously proposed methods for reconstructing dMRI, most of them utilize RPCA or TRPCA to divide dMRI into low rank and sparse parts, while the research on reconstruction using tensor decomposition is still limited. Besides, most current approaches such as [27], [33], [34] focus on preserving global information better, and the local details reconstruction is without consideration. Meanwhile, the global constraints in the low-rank term \mathcal{L} are mostly based on the convex substitution of tucker rank, which expands the tensor along each dimension and computes the nuclear norm of the unfolding matrices. Nevertheless, this way would destroy the structural information of the tensor.

In this subsection, we utilize the TNN as the global low rank constraint to provide a tighter convex substitution of tensor

rank. Meanwhile, for the acquisition of singular values, instead of the usual t-SVD, the tensor QR decomposition-based trifactORIZATION method is utilized to obtain a lower triangular tensor with a smaller dimension rather than the original tensor as the optimization objective in the TNN minimization term. In addition, considering the significance of details variation, we enforce the asymmetric total variation regularizer term as compensation to enhance the local detail recovery of dMRI. Different from the commonly used TV regularizer, asymmetric total variation assigns different smoothing strengths to differences of spatial and temporal dimensions. The reason is that dMRI data should have different smoothing strengths in the spatial and temporal dimensions. Therefore, asymmetric total variation facilitates better utilization of spatio-temporal information and more flexible recovery of dMRI data. Based on the above discussion, our TQRTV model could be represented as

$$\min_{\mathcal{X}, \mathcal{L}, \mathcal{D}, \mathcal{R}} \frac{1}{2} \|\mathbb{T}(\mathcal{X}) - \mathcal{A}\|_F^2 + \lambda_1 \|\mathcal{D}\|_* + \lambda_2 \|\mathcal{X}\|_{ATV}, \quad (7)$$

$$s.t. \mathcal{X} = \mathcal{L} * \mathcal{D} * \mathcal{R}, \mathcal{P}_\Omega(\mathcal{L} * \mathcal{D} * \mathcal{R}) = \mathcal{P}_\Omega(\mathcal{A}),$$

where $\mathcal{L} \in \mathbb{R}^{n_1 \times r \times n_3}$, $\mathcal{R} \in \mathbb{R}^{r \times n_2 \times n_3}$, and $\mathcal{D} \in \mathbb{R}^{r \times r \times n_3}$ are obtained by T-QR; λ_1 and λ_2 indicate the regularization parameters; $\|\mathcal{D}\|_*$ represents the tensor nuclear norm defined in (1). $\|\mathcal{X}\|_{ATV}$ represents the asymmetric three dimensional total variation regularizer, which imposes different smoothing strengths on spatial and temporal dimensions to capture the detailed information of different dimensions and is formulated as

$$\|\mathcal{X}\|_{ATV} = \sum_{i=\{h,v,z\}} \beta_i \|D_i \mathcal{X}\|_1 \quad (8)$$

$$= \beta_h \|D_h \mathcal{X}\|_1 + \beta_v \|D_v \mathcal{X}\|_1 + \beta_z \|D_z \mathcal{X}\|_1,$$

where D_h , D_v , D_z represent difference operators along horizontal, vertical and spectral dimensions, respectively; β_h , β_v , β_z denote the weights on three dimensions to flexibly exploit the smoothness of each direction. The three first-order difference operators in Eq. (8) can be calculated as

$$\begin{cases} (D_h \mathcal{X})_{ijk} = \mathcal{X}_{i+1,jk} - \mathcal{X}_{ijk} \\ (D_v \mathcal{X})_{ijk} = \mathcal{X}_{i,j+1,k} - \mathcal{X}_{ijk} \\ (D_z \mathcal{X})_{ijk} = \mathcal{X}_{ij,k+1} - \mathcal{X}_{ijk} \end{cases} \quad (9)$$

Different from existing dMRI recovery methods such as [27], [33], [34], (1) the proposed TQRTV model utilizes the T-QR decomposition instead of the original t-SVD; (2) the proposed TQRTV model exploits not only the global low-rank tensor nature of dMRI data, but also the local structural details. These global and local information are updated in a mutually promotional way.

B. Optimization Procedure

According to Eq. (8), we can rewrite Eq. (7) as

$$\min_{\mathcal{X}, \mathcal{L}, \mathcal{D}, \mathcal{R}} \frac{1}{2} \|\mathbb{T}(\mathcal{X}) - \mathcal{A}\|_F^2 + \lambda_1 \|\mathcal{D}\|_* + \lambda_2 \sum_{i=\{h,v,z\}} \beta_i \|D_i \mathcal{X}\|_1, \quad (10)$$

$$s.t. \mathcal{X} = \mathcal{L} * \mathcal{D} * \mathcal{R}, \mathcal{P}_\Omega(\mathcal{L} * \mathcal{D} * \mathcal{R}) = \mathcal{P}_\Omega(\mathcal{A}).$$

Here we utilize the ADMM algorithm to tackle the optimization problem (10). First, we convert the above constrained problem into an unconstrained one as follows:

$$L(\mathcal{X}, \mathcal{L}, \mathcal{D}, \mathcal{R}, \mathcal{Y})$$

$$= \frac{1}{2} \|\mathbb{T}(\mathcal{X}) - \mathcal{A}\|_F^2 + \lambda_1 \|\mathcal{D}\|_* + \lambda_2 \sum_{i=\{h,v,z\}} \beta_i \|D_i \mathcal{X}\|_1$$

$$+ \langle \mathcal{Y}, \mathcal{X} - \mathcal{L} * \mathcal{D} * \mathcal{R} \rangle + \frac{\mu}{2} \|\mathcal{X} - \mathcal{L} * \mathcal{D} * \mathcal{R}\|_F^2, \quad (11)$$

where \mathcal{Y} denotes the Lagrange multiplier and μ represents a penalty parameter. For the above issue, we can solve it by alternately iterating several subproblems with ADMM framework.

1) *Update \mathcal{L} and \mathcal{R}* : By fixing the rest of variables, we can get the \mathcal{L} subproblem as

$$\mathcal{L}_{l+1} = \arg \min_{\mathcal{L}} \left\| \mathcal{X}_l - \mathcal{L} * \mathcal{D}_l * \mathcal{R}_l + \frac{\mathcal{Y}_l}{\mu_l} \right\|_F^2. \quad (12)$$

Here we do not follow the steps of solution in ADMM, but introduce CTSVD-QR to optimize the subproblem. The advantage of this is that accurate and fast CTSVD-QR decomposition can speed up the convergence. Then, the \mathcal{L}_{l+1} problem can be obtained by

$$[\hat{\mathcal{L}}_{l+1}, \sim] = \text{T-QR}((\mathcal{X}_l + \frac{\mathcal{Y}_l}{\mu_l}) * \mathcal{R}_l^T) \quad (13)$$

$$\mathcal{L}_{l+1} = \hat{\mathcal{L}}_{l+1}(:, 1:r, :),$$

where $r > 0$ represents the pre-estimated tube rank, and T-QR denotes the tensor Qatar Riyal decomposition. Similarly, we can give the variable \mathcal{R}_{l+1} by CTSVD-QR as follows:

$$[\hat{\mathcal{R}}_{l+1}, \tilde{\mathcal{D}}_l] = \text{T-QR}((\mathcal{X}_l + \frac{\mathcal{Y}_l}{\mu_l})^T * \mathcal{L}_{l+1}) \quad (14)$$

$$\mathcal{R}_{l+1} = \hat{\mathcal{R}}_{l+1}(:, 1:r, :)^T.$$

To sum up, the tensor $\mathcal{X}_l + \mathcal{Y}_l/\mu_l$ is utilized as the input of CTSVD-QR, then we get \mathcal{L}_{l+1} , \mathcal{R}_{l+1} and $\tilde{\mathcal{D}}_l$, where $\tilde{\mathcal{D}}_l$ would be utilized when updating \mathcal{D} in the next step. Therefore, we can summarize this decomposition as the following equation:

$$\mathcal{X}_l + \frac{\mathcal{Y}_l}{\mu_l} = \mathcal{L}_{l+1} * \hat{\mathcal{D}}_l * \mathcal{R}_{l+1}, \quad (15)$$

where $\hat{\mathcal{D}}_l = \tilde{\mathcal{D}}_l(1:r, 1:r, :)^T$. Based on this, the $\hat{\mathcal{D}}_l$ can be written as

$$\hat{\mathcal{D}}_l = \mathcal{L}_{l+1}^T * \left(\mathcal{X}_l + \frac{\mathcal{Y}_l}{\mu_l} \right) * \mathcal{R}_{l+1}^T. \quad (16)$$

2) *Update \mathcal{D}* : We fix the rest of variables, and express the \mathcal{D} subproblem as

$$\mathcal{D}_{l+1} = \arg \min_{\mathcal{D}} \lambda_1 \|\mathcal{D}\|_*$$

$$+ \frac{\mu_l}{2} \left\| \mathcal{X}_l - \mathcal{L}_{l+1} * \mathcal{D} * \mathcal{R}_{l+1} + \frac{\mathcal{Y}_l}{\mu_l} \right\|_F^2. \quad (17)$$

For solving \mathcal{D} , we multiply the second term by \mathcal{L}_{l+1}^T on the left and \mathcal{R}_{l+1}^T on the right at the same time. According to the

nature of the orthogonal tensor, we can rewrite the problem (17) as

$$\begin{aligned} \mathcal{D}_{l+1} = \arg \min_{\mathcal{D}} \lambda_1 \|\mathcal{D}\|_* \\ + \frac{\mu_l}{2} \left\| \mathcal{D} - \mathcal{L}_{l+1}^T * \left(\mathcal{X}_l + \frac{\mathcal{Y}_l}{\mu_l} \right) * \mathcal{R}_{l+1}^T \right\|_F^2. \end{aligned} \quad (18)$$

According to Eq. (16) mentioned above, we can reformulate the problem (17) as

$$\mathcal{D}_{l+1} = \arg \min_{\mathcal{D}} \lambda_1 \|\mathcal{D}\|_* + \frac{\mu_l}{2} \left\| \mathcal{D} - \hat{\mathcal{D}}_l \right\|_F^2. \quad (19)$$

The problem (19) can utilize the singular value thresholding (SVT) [53] to obtain a closed-form solution, *i.e.*,

$$\mathcal{D}_{l+1} = \text{SVT}_{\frac{\lambda_1}{\mu_l}} \left(\hat{\mathcal{D}}_l \right), \quad (20)$$

where SVT is an operator which is defined as $\text{SVT}_{\theta}(\mathcal{P}) = \mathcal{U} * \mathcal{S}_{\theta} * \mathcal{V}^T$, and $\mathcal{S}_{\theta} = \text{ift} \left((\bar{\mathcal{S}} - \theta)_+, \cdot, 3 \right)$.

3) *Update \mathcal{X}* : We fix the rest of variables, and express the \mathcal{X} subproblem as

$$\begin{aligned} \min_{\mathcal{X}} \frac{1}{2} \|\mathbb{T}(\mathcal{X}) - \mathcal{A}\|_F^2 + \lambda_2 \sum_{i=\{h,v,z\}} \beta_i \|D_i \mathcal{X}\|_1 \\ + \frac{\mu_l}{2} \left\| \mathcal{X} - \mathcal{L}_{l+1} * \mathcal{D}_{l+1} * \mathcal{R}_{l+1} + \frac{\mathcal{Y}_l}{\mu_l} \right\|_F^2 \\ = \min_{\mathcal{X}} \frac{1}{2} \|\mathfrak{R}(\mathcal{X}) - \mathcal{R}\|_F^2 + \lambda_2 \sum_{i=\{h,v,z\}} \beta_i \|D_i \mathcal{X}\|_1, \end{aligned} \quad (21)$$

where

$$\begin{cases} \mathfrak{R}(\mathcal{X}) = \mathbb{T}^{-1} \mathbb{T}(\mathcal{X}) + \mu_l \mathcal{X} \\ \mathcal{R} = \mathbb{T}^{-1} \mathcal{A} + \mu_l (\mathcal{L}_{l+1} * \mathcal{D}_{l+1} * \mathcal{R}_{l+1}) - \mathcal{Y}_l \end{cases}.$$

For tackling the above problem, we introduce the primal dual algorithm [54]. Utilizing the Legendre Frechel transformation, we can rewrite the problem (21) as

$$\begin{aligned} \min_{\mathcal{X}} \max_{\mathcal{N}_0, \mathcal{N}_1, \mathcal{N}_2, \mathcal{N}_3} \Gamma(\mathcal{X}, \mathcal{N}_0, \mathcal{N}_1, \mathcal{N}_2, \mathcal{N}_3) \\ = \min_{\mathcal{X}} \max_{\mathcal{N}_0, \mathcal{N}_1, \mathcal{N}_2, \mathcal{N}_3} \langle \mathfrak{R}(\mathcal{X}) - \mathcal{R}, \mathcal{N}_0 \rangle - \frac{1}{2} \|\mathcal{N}_0\|_F^2 \\ + \langle D_h \mathcal{X}, \mathcal{N}_1 \rangle + \langle D_v \mathcal{X}, \mathcal{N}_2 \rangle + \langle D_z \mathcal{X}, \mathcal{N}_3 \rangle, \end{aligned} \quad (22)$$

where the $\mathcal{N}_0, \mathcal{N}_1, \mathcal{N}_2, \mathcal{N}_3$ represents the dual variables, whose dimensions remain the same as \mathcal{X} . Meanwhile, $\mathcal{N}_1, \mathcal{N}_2, \mathcal{N}_3$ must satisfy the conditions:

$$\|\mathcal{N}_1\|_{\infty} \leq \lambda_2 \beta_h, \|\mathcal{N}_2\|_{\infty} \leq \lambda_2 \beta_v, \|\mathcal{N}_3\|_{\infty} \leq \lambda_2 \beta_z. \quad (23)$$

Then, by utilizing the gradient descent algorithm, we can

obtain:

$$\begin{aligned} \frac{\mathcal{N}_1(l+1) - \mathcal{N}_1(l)}{\varepsilon} &= \nabla_{\mathcal{N}_1} \Gamma(\mathcal{X}, \mathcal{N}_0, \mathcal{N}_1, \mathcal{N}_2, \mathcal{N}_3) = D_h \mathcal{X}, \\ \frac{\mathcal{N}_2(l+1) - \mathcal{N}_2(l)}{\varepsilon} &= \nabla_{\mathcal{N}_2} \Gamma(\mathcal{X}, \mathcal{N}_0, \mathcal{N}_1, \mathcal{N}_2, \mathcal{N}_3) = D_v \mathcal{X}, \\ \frac{\mathcal{N}_3(l+1) - \mathcal{N}_3(l)}{\varepsilon} &= \nabla_{\mathcal{N}_3} \Gamma(\mathcal{X}, \mathcal{N}_0, \mathcal{N}_1, \mathcal{N}_2, \mathcal{N}_3) = D_z \mathcal{X}, \\ \frac{\mathcal{N}_0(l+1) - \mathcal{N}_0(l)}{\varepsilon} &= \nabla_{\mathcal{N}_0} \Gamma(\mathcal{X}, \mathcal{N}_0, \mathcal{N}_1, \mathcal{N}_2, \mathcal{N}_3) \\ &= \mathfrak{R}(\mathcal{X}_l) - \mathcal{R} - \mathcal{N}_0(l+1), \\ \frac{\mathcal{X}_{l+1} - \mathcal{X}_l}{\varphi} &= \nabla_{\mathcal{X}} \Gamma(\mathcal{X}, \mathcal{N}_0, \mathcal{N}_1, \mathcal{N}_2, \mathcal{N}_3) \\ &= D_h^T \mathcal{N}_1 + D_v^T \mathcal{N}_2 + D_z^T \mathcal{N}_3 + \mathfrak{R}^{-1}(\mathcal{N}_0), \end{aligned} \quad (24)$$

where ε and φ are the update step size. We set $\varepsilon = \varphi = 1/\sqrt{15}$ in our experiments.

According to Eq. (23), the element-wise projection operator is written as

$$\text{proj}_{\omega}(\mathcal{P}_{ijk}) = \frac{\mathcal{P}_{ijk}}{\max \left\{ 1, \frac{|\mathcal{P}_{ijk}|}{\omega} \right\}}, \quad (25)$$

then we can update the variables as follows:

$$\mathcal{N}_1(l+1) = \text{proj}_{\lambda_2 \beta_h} (\mathcal{N}_1(l) + \varepsilon D_h \mathcal{X}_l), \quad (26)$$

$$\mathcal{N}_2(l+1) = \text{proj}_{\lambda_2 \beta_v} (\mathcal{N}_2(l) + \varepsilon D_v \mathcal{X}_l), \quad (27)$$

$$\mathcal{N}_3(l+1) = \text{proj}_{\lambda_2 \beta_z} (\mathcal{N}_3(l) + \varepsilon D_z \mathcal{X}_l), \quad (28)$$

$$\mathcal{N}_0(l+1) = \frac{\mathcal{N}_0(l) + \varepsilon \mathfrak{R}(\mathcal{X}_l) - \mathcal{R}}{1 + \varepsilon}, \quad (29)$$

$$\begin{aligned} \mathcal{X}_{l+1} = \mathcal{P}_{\Omega^c}(\mathcal{X}_l - \varphi (D_h^T \mathcal{N}_1 + D_v^T \mathcal{N}_2 + D_z^T \mathcal{N}_3 \\ + \mathfrak{R}^{-1}(\mathcal{N}_0))) + \mathcal{P}_{\Omega}(\mathcal{A}), \end{aligned} \quad (30)$$

where Ω^c represents the complementary set of Ω . The steps of solving \mathcal{X} are outlined in Algorithm 1. Meanwhile, we introduce the extended Nesterov's method, which is also used in [55], [56], to speed up the Algorithm 1.

Algorithm 1 : Update \mathcal{X}

Input: $\mathcal{X}, \mathcal{N}_0, \mathcal{N}_1, \mathcal{N}_2, \mathcal{N}_3, D_h, D_v, D_z, \varepsilon, \varphi$

- 1: Update $\mathcal{N}_1(l+1)$ via (26);
- 2: Update $\mathcal{N}_2(l+1)$ via (27);
- 3: Update $\mathcal{N}_3(l+1)$ via (28);
- 4: Update $\mathcal{N}_0(l+1)$ via (29);
- 5: calculate \mathcal{X}_{old} via (30);
- 6: calculate $\mathcal{X}_{l+1} = 2\mathcal{X}_{old(l+1)} - \mathcal{X}_{old(l)}$;

Output: \mathcal{X} .

4) *Update \mathcal{Y} and μ* : The multiplier and parameter can be updated by

$$\mathcal{Y}_{l+1} = \mathcal{Y}_l + \mu_l (\mathcal{X}_{l+1} - \mathcal{L}_{l+1} \mathcal{D}_{l+1} \mathcal{R}_{l+1}) \quad (31)$$

$$\mu_{l+1} = \min \{ \alpha * \mu_l, \mu_{\max} \}, \quad (32)$$

where α is a constant, and μ_{\max} denotes the maximum value of the parameter μ .

Algorithm 2 : The proposed TQRTV for dMRI reconstruction

Input: $\mathcal{A}, \xi, \varepsilon, \varphi$

Initialization: $l = 0, \mathcal{L}_0 = \mathcal{I}, \mathcal{D}_0 = \mathcal{I}, \mathcal{R}_0 = \mathcal{I}, \mathcal{X}_0 = \mathcal{A}, \mathcal{Y}_0 = \mathcal{X}_0, \mathcal{N}_{1(0)} = \mathcal{N}_{2(0)} = \mathcal{N}_{3(0)} = \mathcal{N}_{0(0)} = \text{zeros}(\text{size}(\mathcal{X}))$.

- 1: **while** $\|\mathcal{X}_{l+1} - \mathcal{X}_l\|_F / \|\mathcal{A}\|_F \leq \xi$ **do**
- 2: Update \mathcal{L}_{l+1} via (13);
- 3: Update \mathcal{R}_{l+1} via (14);
- 4: Update \mathcal{D}_{l+1} via (20);
- 5: Update \mathcal{X}_{l+1} via Algorithm 1;
- 6: Update \mathcal{Y}_{l+1} via (31);
- 7: Update μ_{l+1} via (32);
- 8: **end while**

Output: \mathcal{X} .

C. Computational Complexity

The proposed TQRTV algorithm is outlined in Algorithm 2. Since our TQRTV algorithm contains four block variables, it is difficult to give a detailed convergence analysis. Fortunately, we can observe the numerical convergence as shown in Fig. 15.

In this section, we also discuss the computational complexity of the proposed TQRTV model. The time for updating \mathcal{L} and \mathcal{R} is mainly consumed on the FFT, inverse FFT, matrix product and QR decomposition, and the complexity is $O(r(n_1 + n_2)n_3 \log n_3 + rn_1n_2n_3)$, where $r \leq \min\{n_1, n_2\}$ is the estimated tubal rank. The complexity of computing subproblem \mathcal{D} is $O(r^2n_3 \log n_3)$. The time for updating \mathcal{X} and \mathcal{Y} is mainly consumed on the calculation of the projection operator, sampling operator, and tensor product, and the computational cost of the two steps is $O(r(n_1 + n_2)n_3 \log n_3 + n_1n_2n_3 + r^3n_3)$. Thus, the total cost of TQRTV is bounded by $O(r(n_1 + n_2)n_3 \log n_3 + rn_1n_2n_3 + r^3n_3)$.

IV. NUMERICAL EXPERIMENTS

A. Experimental Settings

Here we implement extensive experiments on phantom data and single-coil dynamic MRI Data to verify the effectiveness of our proposed TQRTV method. Datasets are then undersampled using the radial sampling schemes in k-space, which takes sample along the lines on spatial dimensions with different angles and is fully sampled on the time dimension [57]. We show the radial sampling scheme in Fig. 3.

The proposed TQRTV will be implemented on the phantom dataset and two single-coil dynamic MRI datasets. TQRTV is compared with some existing dMRI reconstruction approaches, including STRPCA [33], TMNN [40], FTVNRR [14], [15], and k-t RPCA [27]. Here, k-t RPCA is the typical RPCA-based method. STRPCA and TMNN are recently proposed low-rank tensor-based methods. FTVNRR is the approach based on the low-rank matrix approximation and total variation. In addition to the above methods, we also add a deep learning-based method on the two real single-coil dynamic MRI datasets to further verify the performance of the proposed method. The method is abbreviated to FM3D-CSC

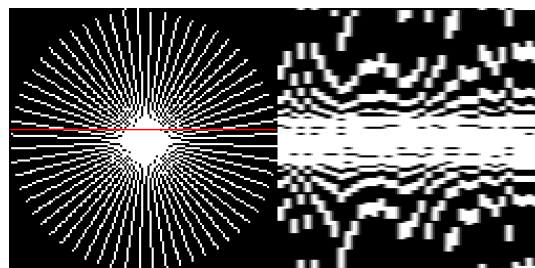


Fig. 3: The illustration of the radial sampling (left) and the time profile along the line (right).

[44], which combines three-dimensional convolutional filters in various scales and elastic net regularization.

To specify the performance of our TQRTV method and other competitors, the sampling rate (SR) is denoted as

$$SR = \frac{O}{n_1 \times n_2 \times n_3},$$

where O indicates the number of sampled pixels. The performance of all methods in our experiments are quantified using the root mean square error (RMSE) and the peak signal noise ratio (PSNR). The RMSE is formulated as

$$RMSE(X_{Rec}) = \sqrt{\frac{\|X_{Rec} - X_F\|_F^2}{n_1 \times n_2}},$$

where X_{Rec} denotes the recovered frames of dynamic MRI and X_F denotes the unbroken frames of dynamic MRI. We utilize the mean of the RMSE over all frames of the dMRI to evaluate the recovery accuracy. In addition, the PSNR is defined as

$$PSNR(\mathcal{X}_{Rec}) = 10 \log_{10} \frac{\text{Max}_{\mathcal{X}_{Rec}, \mathcal{X}_F}^2}{\|\mathcal{X}_{Rec} - \mathcal{X}_F\|_F^2},$$

where \mathcal{X}_{Rec} and \mathcal{X}_F indicate the recovered and fully sampled dMRI data. The PSNR here is utilized to assess the global recovery accuracy. The experiments are carried out on the platform of Windows 10 with an Intel(R) Core (TM) i9-10900 CPU at 3.70GHz and 64GB RAM.

B. Experimental Results

1) **Phantom Data:** We verify the superiority of the proposed TQRTV on the PINCAT perfusion phantom data with dynamics because of the cardiac perfusion uptake and breathing motion [7], [58], which has dimensions of $128 \times 128 \times 50$ [59].

Fig. 4 shows the average PSNR values by all methods on PINCAT data with different sampling rate. We can find that our proposed method is inferior to TMNN and FTVNRR at low sampling rate. However, the curve slope of the proposed TQRTV varies drastically. As the sampling rate increases, the proposed approach is more efficient and outperforms all other methods. In Fig. 5, we also plot the PSNR line chart of each recovered time frame at the SR=0.25. As observed, the proposed TQRTV achieves superior PSNR values on almost all time frames, which also illustrates the robustness of TQRTV on different temporal frames of the phantom cycle.

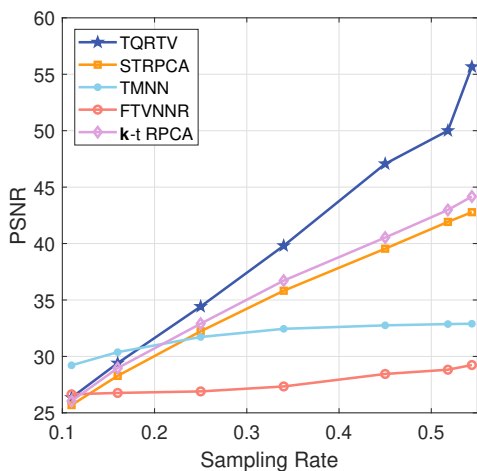


Fig. 4: The PSNR values of the reconstructed PINCAT dataset with different SR.

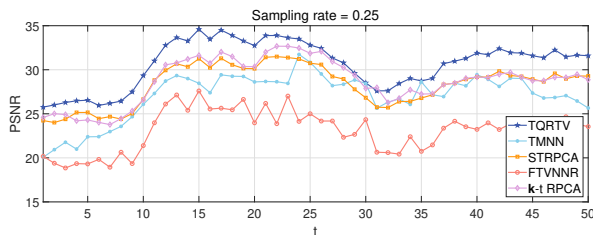


Fig. 5: The PSNR values of each time frame on PINCAT dataset at the sampling rate of 0.25.

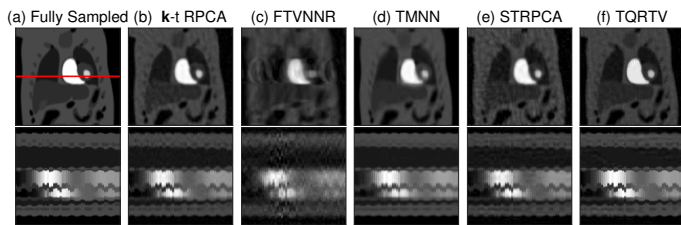


Fig. 6: The first row is a contrast of the recovery performance from all approaches on the 18-th frame of the PINCAT dataset. The 64-th time profile of the corresponding recovered image is shown in the second row.

To demonstrate the recovery performance of all approaches more intuitively, Fig. 6 shows the visual effects of the recovered results of all approaches on the 18-th frame at the radial SR=0.25. Meanwhile, the 64-th time profile of the corresponding recovered image is displayed in the second row of Fig. 6. We can find that the FTVNMR method suffers from blurring and artifacts, and the image recovered by the TMNN method is excessively smooth. Obviously, our proposed approach achieves the optimal recovery performance compared to other competing approaches.

2) *Single-Coil Dynamic MRI Data*: In this subsection, two dynamic MRI datasets, including a cardiac cine dataset with size of $256 \times 256 \times 30$ from [60], and an in-vivo cardiac perfusion MRI dataset with size of $128 \times 128 \times 40$ from [7]

are utilized to prove the effectiveness of the proposed TQRTV. Similar to the previous simulation, the radial sampling scheme is also adopted to sample the two complex-valued cardiac datasets.

First, the cardiac cine dataset is utilized to contrast reconstruction performance. We plot the average PSNR and average RMSE curves with respect to different sample rates in Fig. 7. Although the reconstruction performance of the FM3D-CSC, STRPCA and TMNN methods is close to that of our TQRTV at low sampling rate, it is obvious that our TQRTV method increases the PSNR more rapidly. To further illustrate the superiority of our proposed TQRTV, we plot the PSNR values of each time frame on cardiac cine data at SR=0.25 in Fig. 8. As observed, our proposed approach can achieve the most excellent performance on all frames, which also confirms the superiority of the proposed QR decomposition and asymmetric total variation-based model for dMRI reconstruction.

More intuitively, Fig. 9 shows the visual effects of the recovery results of different methods, where the first row is the comparison of the reconstruction results of different methods on the 15-th frame of the cardiac cine data, and the 95-th time profile of the corresponding recovered image is shown in the second row. We observed that k-t RPCA, FTVNMR, TMNN still have some blurring artifacts. FM3D-CSC loses a small amount of information in the details. Meanwhile, although the reconstruction results of STRPCA and TQRTV are close, our method preserves more edge details. This further illustrates that the singular values of the tensor QR decomposition are the corking characteristics of dynamic MRI data.

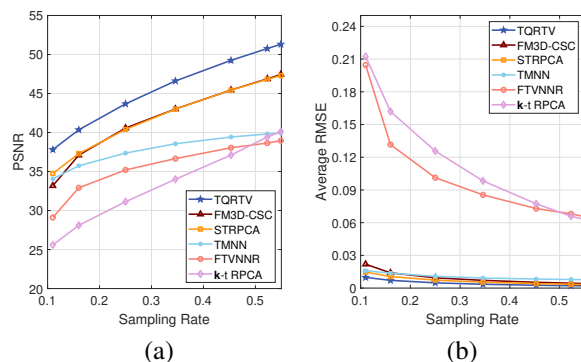


Fig. 7: (a) The PSNR values of the recovered cardiac cine data with different SR. (b) The average RMSE values of the recovered cardiac cine data with different SR.

Then, the cardiac perfusion dataset is utilized to contrast reconstruction performance. Fig. 10 shows the average PSNR and average RMSE values of the recovered perfusion dynamic MRI data using radial sampling pattern. It can be found that our approach can achieve the most excellent performance at most sampling rates. The proposed method is inferior to TMNN with sampling rate of 0.11. The reason may be that the QR decomposition is not stable enough when the amount of information is too sparse. Moreover, we plot the PSNR values of each time frame on cardiac perfusion data at the SR=0.25 in Fig. 11. It is not difficult to find that our method significantly

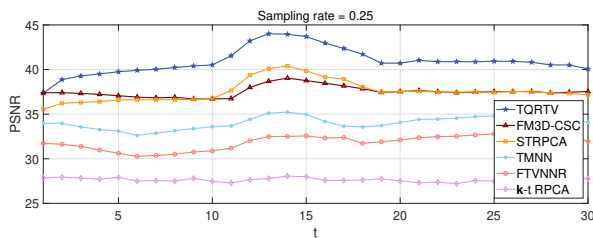


Fig. 8: The PSNR values of each time frame on cardiac cine dataset at the SR=0.25.

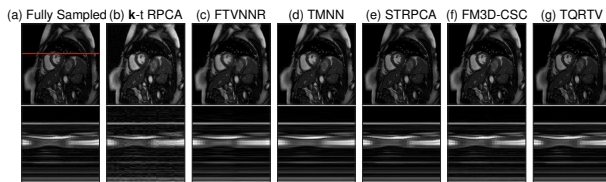


Fig. 9: The first row is a contrast of the recovery performance from all approaches on the 15-th frame of the cardiac cine dataset. The 95-th temporal profile of the corresponding recovered frame is shown in the second row.

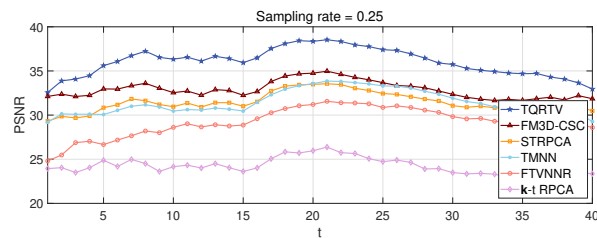


Fig. 11: The PSNR values of each time frame on cardiac perfusion dataset at the SR=0.25.

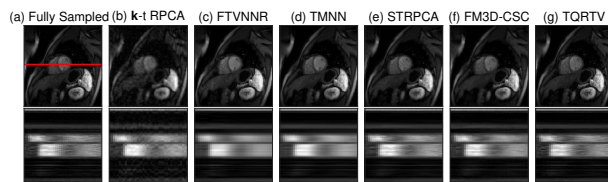


Fig. 12: The first row is a contrast of the recovery performance from all approaches on the 20-th frame of the cardiac perfusion dataset. The 62-th temporal profile of the corresponding recovered frame is shown in the second row.

outperforms other methods and is robust to different time frames.

For visual comparison, Fig. 12 shows the recovery results from different methods on the 20-th frame of the cardiac perfusion data at the SR=0.25. The 62-th time profile of the corresponding recovered image is displayed in the second row of Fig. 12. We found that *k-t* RPCA, FTVNNR, and TMNN still have artifacts and are relatively blurry. STRPCA and FM3D-CSC have better results, while our method recovers the most boundaries and details.

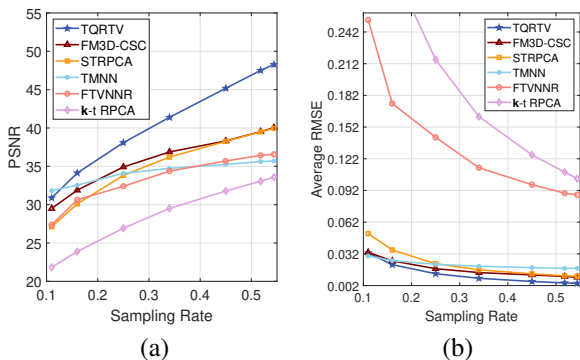


Fig. 10: (a) The PSNR values of the reconstructed cardiac perfusion data with different sampling rates. (b) The average RMSE values of the recovered cardiac perfusion data with different SR.

C. Parameter Analysis

In our proposed model, the following parameters are considered. The parameter r represents the estimated tensor tubal rank of the data \mathcal{X} . For PINCAT and cardiac perfusion datasets, we set it to 30, and for cardiac cine dataset we set it to

50. The parameters λ_1 and λ_2 are utilized to adjust the balance among the different regularization terms; the $\beta_h, \beta_v, \beta_z$ are used to control the weights of smooth strength in different dimensions. In the next experiments, we will report the effect of $\lambda_1, \lambda_2, \beta_h, \beta_v, \beta_z$ on the cardiac cine dataset at sampling rate of 0.25.

In Table I, we set λ_1 to range from $1e-4$ to 1, and λ_2 to range from $1e-4$ to $1e-1$. While in Table II, β_h and β_v to range from $1e-4$ to 1, β_z to range from 1 to 4. We only change one parameter at a time, while the rest are set to the optimal values. Table I and Table II report the PSNR values of the proposed method on cardiac cine dataset for different values of $\lambda_1, \lambda_2, \beta_h, \beta_v, \beta_z$. From Table I, it can be found that the proposed approach achieves the optimal result when $\lambda_1 = 1e-1$ and $\lambda_2 = 1e-3$. Meanwhile, the change of λ_2 has a greater impact on the final performance than that of λ_1 , which also shows that an appropriate total variation regularizer term is beneficial to the dMRI reconstruction. In Table II, the optimal result is achieved when $\beta_h = \beta_v = 1e-1$ and $\beta_z = 2$. It can be observed that the asymmetric total variation can achieve better reconstruction performance than the usual total variation term with $\beta_h = \beta_v = \beta_z = 1$. Similarly, we have also conducted parameter experiments on the cardiac perfusion and PINCAT datasets, and obtained the optimal parameter settings as $\lambda_1 = 1e-1, \lambda_2 = 1e-3, \beta_h = \beta_v = 1e-1$ and $\beta_z = 4$. Due to space limitations and similar experimental settings, we will not list them here.

D. Ablation Experiments

To show the effectiveness of the proposed method that integrates the T-QR decomposition, the TNN, and asymmetric total variation, we discuss the contributions of T-QR decomposition, the TNN, and asymmetric total variation on the cardiac cine dataset with different sampling rates. Fig. 13 shows the

TABLE I: PSNR Values of the Proposed Method on Cardiac Cine Dataset for Different Values of λ_1 , and λ_2

		λ_1				
		1e-4	1e-3	1e-2	1e-1	1
λ_2	1e-4	36.3409	36.3420	36.3434	36.3637	36.5013
	1e-3	44.4449	44.4484	44.4467	44.4710	44.5449
	1e-2	41.2029	41.2075	41.2073	41.2206	41.2444
	1e-1	30.2549	30.2586	30.2622	30.2683	30.3516

TABLE II: PSNR Values of the Proposed Method on Cardiac Cine Dataset for Different Values of β_h , β_v , and β_z

		β_h, β_v				
		1e-4	1e-3	1e-2	1e-1	1
β_z	1	41.5803	41.6109	41.9021	43.5222	41.0885
	2	43.7590	43.7772	43.9454	44.6896	42.3995
	3	43.8256	43.8362	43.9345	44.4133	42.8222
	4	43.5665	43.5738	43.6424	44.0208	42.9346

PSNR and RMSE values of the proposed method and the comparison methods TQR+TNN and TNN at different sampling rates. It can be found that at low sampling rates, the PSNR and RMSE values of the TQR+TNN method are slightly inferior to TNN. The reason may be that the TQR decomposition is not stable enough when there are too few available elements. As the sampling rate increases, the TQR+TNN method shows a substantial improvement. Obviously, the proposed TQRTV has promising performance compared to the other two comparison methods, which also illustrates the important role of the asymmetric TV regularization in recovering detailed textures. The visual performance comparison of the recovery results is plotted in Fig. 14. We can observe that there exist block-artifacts in the result of TNN method. By applying T-QR decomposition on TNN, the reconstruction results are significantly improved in terms of details. We can observe that the corresponding result with the most detail by the proposed TQRTV is superior to other methods and is the closest to the ground truth.

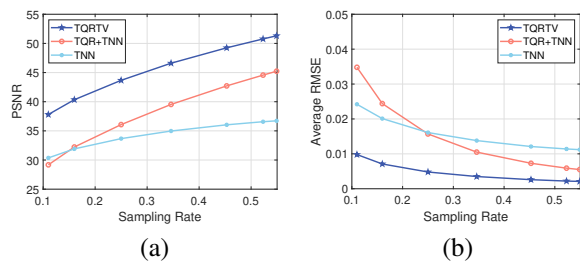


Fig. 13: (a) The PSNR values of the reconstructed cardiac cine data with different sampling rates. (b) The average RMSE values of the recovered cardiac cine data with different sampling rates.

TABLE III: Running Time (in Seconds) of the Proposed and Competing Methods

k-t RPCA	FTVNNR	TMNN	STRPCA	FM3D-CSC	TQRTV
11.48	41.12	4.02	138.62	200.25	156.71

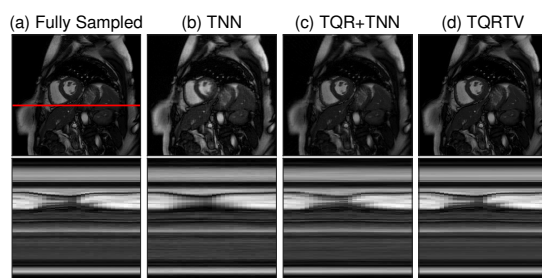


Fig. 14: The first row is a contrast of the recovery performance from all approaches on the 15-th frame of the cardiac cine dataset. The 150-th temporal profile of the corresponding recovered frame is shown in the second row.

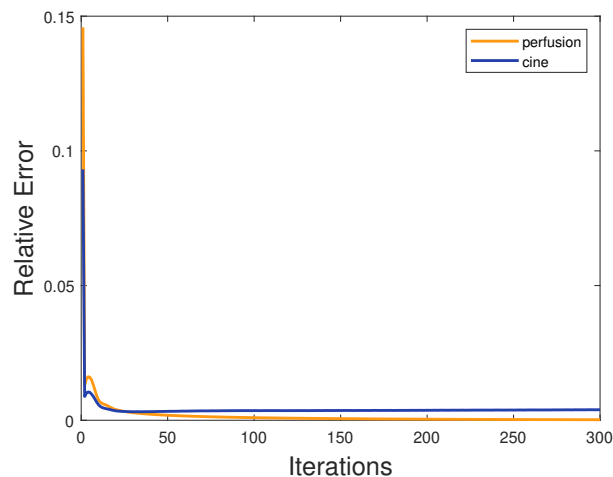


Fig. 15: The convergence curves on cardiac cine and cardiac perfusion datasets.

E. Convergence Behaviors and Running Time

Fig. 15 shows the convergence curves on cardiac cine and cardiac perfusion datasets. The accuracy performance in each iteration can be objectively measured by the relative error (RE) of the ordinate, which is defined as $RE = (\|\mathcal{X}_{l+1}\|_F - \|\mathcal{X}_l\|_F) / \|\mathcal{X}_l\|_F$. It can be observed that the relative error decreases very rapidly at the beginning of the iteration. After a small fluctuation, there is a stable convergence trend in the subsequent iterations.

We further report the running time of all methods on the cardiac perfusion dataset at SR = 0.25 as shown in Table III. TMNN has the shortest running time since its main calculation consumption is only t-SVD decomposition. The proposed TQRTV is time-consuming due to the need for asymmetric three dimensional total variation calculations. Therefore, the choice of a computationally inexpensive and promising regularizer is still an issue to be considered.

V. CONCLUSION

This paper focused on the dynamic MRI reconstruction and proposed a novel dMRI reconstruction approach by utilizing tensor global and local information. On the one hand, we

utilized the tensor QR decomposition-based tri-factorization method to obtain a lower triangular tensor as an optimization objective for tensor nuclear norm minimization. By doing so, we exploited the low-rank characteristic of dMRI data to reconstruct the global structure. On the other hand, the asymmetric total variation was introduced to capture the slow variation of local details. Then, we solved the proposed model under the ADMM framework. Evaluation experiments are conducted and confirmed that the proposed approach outperforms other state-of-the-art approaches in terms of performance evaluation metrics. However, our method is still plagued by calculation speed due to the cost of total variation. In the future, some more efficient regularizers could be incorporated into the model.

APPENDIX

The CTSVD-QR method is summarized in Algorithm 3.

Algorithm 3 : CTSVD-QR [36], [37]

Input: The matrix $\mathcal{A} \in \mathbb{R}^{n_1 \times n_2 \times n_3}$, the estimated rank r , the indexes of observed pixels Ω , convergence tolerance ξ

```

1: calculate  $\bar{\mathcal{A}} = \text{fft}(\mathcal{A}, [], 3)$ .
2: for  $k = 1, \dots, \lceil \frac{n_3+1}{2} \rceil$  do
3:    $\mathcal{L}^{(k)} = \text{eye}(n_1, r)$ ;  $\mathcal{D}^{(k)} = \text{eye}(r, r)$ ;
4:    $\mathcal{R}^{(k)} = \text{eye}(r, n_2)$ .
5:   while  $\|\mathcal{L}^{(k)}\mathcal{D}^{(k)}\mathcal{R}^{(k)} - \bar{\mathcal{A}}^{(k)}\|_F^2 \leq \xi$  do
6:      $[M, N] = \text{QR}(\bar{\mathcal{A}}^{(k)}(\mathcal{R}^{(k)})^T)$ ;
7:      $\mathcal{L}^{(k)} = M(:, 1:r)$ .
8:      $[M, N] = \text{QR}((\bar{\mathcal{A}}^{(k)})^T\mathcal{L}^{(k)})$ ;
9:      $\mathcal{R}^{(k)} = M(:, 1:r)^T$ .
10:     $\mathcal{D}^{(k)} = N(1:r, 1:r)^T$ .
11:   end while
12: end for
13: for  $k = \lceil \frac{n_3+1}{2} \rceil + 1, \dots, n_3$  do
14:    $\mathcal{L}^{(k)} = \text{conj}(\mathcal{L}^{(n_3-k+2)})$ ;
15:    $\mathcal{D}^{(k)} = \mathcal{D}^{(n_3-k+2)}$ ;
16:    $\mathcal{R}^{(k)} = \text{conj}(\mathcal{R}^{(n_3-k+2)})$ .
17: end for

```

Output: $\hat{\mathcal{L}} = \text{ifft}(\mathcal{L}, [], 3)$, $\hat{\mathcal{D}} = \text{ifft}(\mathcal{D}, [], 3)$,
 $\hat{\mathcal{R}} = \text{ifft}(\mathcal{R}, [], 3)$.

REFERENCES

- [1] R. Gong, X. Han, J. Wang, S. Ying, and J. Shi, "Self-supervised bi-channel transformer networks for computer-aided diagnosis," *IEEE J. Biomed. Health Informat.*, 2022.
- [2] J. Ouyang, Q. Zhao, E. V. Sullivan, A. Pfefferbaum, S. F. Tapert, E. Adeli, and K. M. Pohl, "Longitudinal pooling & consistency regularization to model disease progression from MRIs," *IEEE J. Biomed. Health Informat.*, vol. 25, no. 6, pp. 2082–2092, 2020.
- [3] L. Zhong, Y. Chen, X. Zhang, S. Liu, Y. Wu, Y. Liu, L. Lin, Q. Feng, W. Chen, and W. Yang, "Flexible prediction of ct images from mri data through improved neighborhood anchored regression for pet attenuation correction," *IEEE J. Biomed. Health Informat.*, vol. 24, no. 4, pp. 1114–1124, 2019.
- [4] D. Štern, C. Payer, N. Giuliani, and M. Urschler, "Automatic age estimation and majority age classification from multi-factorial mri data," *IEEE J. Biomed. Health Informat.*, vol. 23, no. 4, pp. 1392–1403, 2018.
- [5] M. Lustig, D. Donoho, and J. M. Pauly, "Sparse MRI: The application of compressed sensing for rapid mr imaging," *Magn. Reson. Med.*, vol. 58, no. 6, pp. 1182–1195, 2007.
- [6] M. Lustig, D. L. Donoho, J. M. Santos, and J. M. Pauly, "Compressed sensing MRI," *IEEE Signal Proc. Mag.*, vol. 25, no. 2, pp. 72–82, 2008.
- [7] S. G. Lingala, Y. Hu, E. DiBella, and M. Jacob, "Accelerated dynamic MRI exploiting sparsity and low-rank structure: k-t SLR," *IEEE Trans. Med. Imag.*, vol. 30, no. 5, pp. 1042–1054, 2011.
- [8] B. Zhao, J. P. Haldar, C. Brinegar, and Z.-P. Liang, "Low rank matrix recovery for real-time cardiac MRI," in *Proc. IEEE Int. Symp. Biomed. Imag.*, pp. 996–999, IEEE, 2010.
- [9] J. P. Haldar and Z.-P. Liang, "Low-rank approximations for dynamic imaging," in *Proc. IEEE Int. Symp. Biomed. Imag.*, pp. 1052–1055, IEEE, 2011.
- [10] X. Liu, J. Yao, X. Hong, X. Huang, Z. Zhou, C. Qi, and G. Zhao, "Background subtraction using spatio-temporal group sparsity recovery," *IEEE Trans. Circuits Syst. Video Technol.*, vol. 28, no. 8, pp. 1737–1751, 2017.
- [11] B. Zhao, J. P. Haldar, A. G. Christodoulou, and Z.-P. Liang, "Image reconstruction from highly undersampled (k, t)-space data with joint partial separability and sparsity constraints," *IEEE Trans. Med. Imag.*, vol. 31, no. 9, pp. 1809–1820, 2012.
- [12] Y. Liu, S. Wu, X. Huang, B. Chen, and C. Zhu, "Hybrid CS-DMRI: Periodic time-variant subsampling and omnidirectional total variation based reconstruction," *IEEE Trans. Med. Imag.*, vol. 36, no. 10, pp. 2148–2159, 2017.
- [13] F. Knoll, K. Bredies, T. Pock, and R. Stollberger, "Second order total generalized variation (TGV) for MRI," *Magn. Reson. Med.*, vol. 65, no. 2, pp. 480–491, 2011.
- [14] J. Yao, Z. Xu, X. Huang, and J. Huang, "An efficient algorithm for dynamic MRI using low-rank and total variation regularizations," *Med. Image Anal.*, vol. 44, pp. 14–27, 2018.
- [15] J. Yao, Z. Xu, X. Huang, and J. Huang, "Accelerated dynamic MRI reconstruction with total variation and nuclear norm regularization," in *Proc. Int. Conf. Med. Image Comput. Comput. Assist. Intervent*, pp. 635–642, Springer, 2015.
- [16] A. G. Christodoulou, T. K. Hitchens, Y. L. Wu, C. Ho, and Z.-P. Liang, "Improved subspace estimation for low-rank model-based accelerated cardiac imaging," *IEEE Trans. Biomed. Eng.*, vol. 61, no. 9, pp. 2451–2457, 2014.
- [17] X. Xiao, Y. Chen, Y.-J. Gong, and Y. Zhou, "Prior knowledge regularized multiview self-representation and its applications," *IEEE Trans. Neural Netw. Learn. Syst.*, vol. 32, no. 3, pp. 1325–1338, 2020.
- [18] X. Liu, G. Zhao, J. Yao, and C. Qi, "Background subtraction based on low-rank and structured sparse decomposition," *IEEE Trans. Image Process.*, vol. 24, no. 8, pp. 2502–2514, 2015.
- [19] E. J. Candès, X. Li, Y. Ma, and J. Wright, "Robust principal component analysis?," *Journal of the ACM (JACM)*, vol. 58, no. 3, pp. 1–37, 2011.
- [20] J. Liu, S. Qiu, N. Luo, S.-K. Lau, H. Yu, T. Kwok, Y.-T. Zhang, and N. Zhao, "PCA-based multi-wavelength photoplethysmography algorithm for cuffless blood pressure measurement on elderly subjects," *IEEE J. Biomed. Health Informat.*, vol. 25, no. 3, pp. 663–673, 2020.
- [21] F. W. Mauldin, D. Lin, and J. A. Hossack, "The singular value filter: A general filter design strategy for pca-based signal separation in medical ultrasound imaging," *IEEE Trans. Med. Imag.*, vol. 30, no. 11, pp. 1951–1964, 2011.
- [22] R. Otazo, E. Candes, and D. K. Sodickson, "Low-rank plus sparse matrix decomposition for accelerated dynamic MRI with separation of background and dynamic components," *Magn. Reson. Med.*, vol. 73, no. 3, pp. 1125–1136, 2015.
- [23] Z. Zha, B. Wen, X. Yuan, S. Ravishanker, J. Zhou, and C. Zhu, "Learning nonlocal sparse and low-rank models for image compressive sensing: Nonlocal sparse and low-rank modeling," *IEEE Signal Processing Magazine*, vol. 40, no. 1, pp. 32–44, 2023.
- [24] Z. Zha, B. Wen, X. Yuan, J. T. Zhou, J. Zhou, and C. Zhu, "Triply complementary priors for image restoration," *IEEE Trans. Image Process.*, vol. 30, pp. 5819–5834, 2021.
- [25] H. Gao, S. Rapacchi, D. Wang, J. Moriarty, C. Meehan, J. Sayre, G. Laub, P. Finn, and P. Hu, "Compressed sensing using prior rank, intensity and sparsity model (PRISM): applications in cardiac cine MRI," in *Proc. Int. Soc. Magn. Reson. Med.*, vol. 2242, 2012.
- [26] H. Gao, L. Li, and X. Hu, "Compressive diffusion MRI—part 2: performance evaluation via low-rank model," in *Proc ISMRM*, vol. 2046, 2013.
- [27] B. Trérouh eac, N. Dikaos, D. Atkinson, and S. R. Arridge, "Dynamic mr image reconstruction—separation from undersampled (k, t)-space via

- low-rank plus sparse prior," *IEEE Trans. Med. Imag.*, vol. 33, no. 8, pp. 1689–1701, 2014.
- [28] C. Y. Lin and J. A. Fessler, "Efficient dynamic parallel MRI reconstruction for the low-rank plus sparse model," *IEEE Trans. Med. Imag.*, vol. 5, no. 1, pp. 17–26, 2018.
- [29] M. Rahmani and G. K. Atia, "High dimensional low rank plus sparse matrix decomposition," *IEEE Trans. Signal Process.*, vol. 65, no. 8, pp. 2004–2019, 2017.
- [30] S. Wang, Y. Chen, Y. Jin, Y. Cen, Y. Li, and L. Zhang, "Error-robust low-rank tensor approximation for multi-view clustering," *Knowl.-Based Syst.*, vol. 215, p. 106745, 2021.
- [31] J. D. Trzasko and A. Manduca, "A unified tensor regression framework for calibrationless dynamic, multi-channel MRI reconstruction," in *Proc. Int. Soc. Magn. Reson. Med.*, p. 603, 2013.
- [32] S. F. Roohi, D. Zonoobi, A. A. Kassim, and J. L. Jaremko, "Multi-dimensional low rank plus sparse decomposition for reconstruction of under-sampled dynamic MRI," *Pattern Recognit.*, vol. 63, pp. 667–679, 2017.
- [33] Y. Liu, T. Liu, J. Liu, and C. Zhu, "Smooth robust tensor principal component analysis for compressed sensing of dynamic MRI," *Pattern Recognit.*, vol. 102, p. 107252, 2020.
- [34] K. Cui, "Dynamic MRI reconstruction via weighted tensor nuclear norm regularizer," *IEEE J. Biomed. Health Informat.*, vol. 25, no. 8, pp. 3052–3060, 2021.
- [35] Z. Zhang, G. Ely, S. Aeron, N. Hao, and M. Kilmer, "Novel methods for multilinear data completion and de-noising based on tensor-SVD," in *Proc. IEEE Conf. Comput. Vis. Pattern Recognit.*, pp. 3842–3849, 2014.
- [36] Q. Liu, F. Davoine, J. Yang, Y. Cui, Z. Jin, and F. Han, "A fast and accurate matrix completion method based on QR decomposition and $l_{2,1}$ -norm minimization," *IEEE Trans. Neural Netw. Learn. Syst.*, vol. 30, no. 3, pp. 803–817, 2018.
- [37] Y. Zheng and A.-B. Xu, "Tensor completion via tensor QR decomposition and $l_{2,1}$ -norm minimization," *Signal Process.*, vol. 189, p. 108240, 2021.
- [38] F. Wu, Y. Li, C. Li, and Y. Wu, "A fast tensor completion method based on tensor QR decomposition and tensor nuclear norm minimization," *IEEE Trans. Comput. Imag.*, vol. 7, pp. 1267–1277, 2021.
- [39] J. Ai, S. Ma, H. Du, and L. Fang, "Dynamic MRI reconstruction using tensor-svd," in *2018 14th IEEE International Conference on Signal Processing (ICSP)*, pp. 1114–1118, IEEE, 2018.
- [40] Y. Zhang and Y. Hu, "Dynamic cardiac MRI reconstruction using combined tensor nuclear norm and casorati matrix nuclear norm regularizations," in *Proc. IEEE Int. Symp. Biomed. Imag.*, pp. 1–4, 2022.
- [41] T. Xu, X. Kong, Q. Shen, Y. Chen, and Y. Zhou, "Deep and low-rank quaternion priors for color image processing," *IEEE Trans. Circuits Syst. Video Technol.*, 2023.
- [42] J. Schlemper, J. Caballero, J. V. Hajnal, A. Price, and D. Rueckert, "A deep cascade of convolutional neural networks for mr image reconstruction," in *International Conference on Information Processing in Medical Imaging*, pp. 647–658, Springer, 2017.
- [43] C. Qin, J. Schlemper, J. Caballero, A. N. Price, J. V. Hajnal, and D. Rueckert, "Convolutional recurrent neural networks for dynamic mr image reconstruction," *IEEE Trans. Med. Imag.*, vol. 38, no. 1, pp. 280–290, 2018.
- [44] T. Nguyen-Duc, T. M. Quan, and W.-K. Jeong, "Frequency-splitting dynamic mri reconstruction using multi-scale 3d convolutional sparse coding and automatic parameter selection," *Medical Image Analysis*, vol. 53, pp. 179 – 196, 2019.
- [45] W. Huang, Z. Ke, Z.-X. Cui, J. Cheng, Z. Qiu, S. Jia, L. Ying, Y. Zhu, and D. Liang, "Deep low-rank plus sparse network for dynamic mr imaging," *Medical Image Analysis*, vol. 73, p. 102190, 2021.
- [46] J. Yang, X. Huang, Y. He, J. Xu, C. Yang, G. X. Xu, and B. Ni, "Reinventing 2d convolutions for 3d images," *IEEE J. Biomed. Health Informat.*, vol. 25, no. 8, pp. 3009–3018, 2021.
- [47] J. Yang, Y. He, K. Kuang, Z. Lin, H. Pfister, and B. Ni, "Asymmetric 3d context fusion for universal lesion detection," in *Proc. Int. Conf. Med. Image Comput. Comput. Assist. Interv.*, pp. 571–580, Springer, 2021.
- [48] M. E. Kilmer, K. Braman, N. Hao, and R. C. Hoover, "Third-order tensors as operators on matrices: A theoretical and computational framework with applications in imaging," *SIAM J. Matrix Anal. Appl.*, vol. 34, no. 1, pp. 148–172, 2013.
- [49] M. E. Kilmer and C. D. Martin, "Factorization strategies for third-order tensors," *Linear Algebra Appl.*, vol. 435, no. 3, pp. 641–658, 2011.
- [50] Y. Liu, L. Jiao, and F. Shang, "A fast tri-factorization method for low-rank matrix recovery and completion," *Pattern Recognit.*, vol. 46, no. 1, pp. 163–173, 2013.
- [51] H. Gudbjartsson and S. Patz, "The rician distribution of noisy MRI data," *Magn. Reson. Med.*, vol. 34, no. 6, pp. 910–914, 1995.
- [52] M. F. Duarte and R. G. Baraniuk, "Kronecker compressive sensing," *IEEE Trans. Image Process.*, vol. 21, no. 2, pp. 494–504, 2011.
- [53] C. Lu, J. Feng, Y. Chen, W. Liu, Z. Lin, and S. Yan, "Tensor robust principal component analysis with a new tensor nuclear norm," *IEEE Trans. Pattern Anal. Mach. Intell.*, vol. 42, no. 4, pp. 925–938, 2019.
- [54] A. Chambolle and T. Pock, "A first-order primal-dual algorithm for convex problems with applications to imaging," *J. Math. Imaging Vis.*, vol. 40, no. 1, pp. 120–145, 2011.
- [55] A. Beck and M. Teboulle, "A fast iterative shrinkage-thresholding algorithm for linear inverse problems," *SIAM J. Imag. Sci.*, vol. 2, no. 1, pp. 183–202, 2009.
- [56] J. Huang, S. Zhang, and D. Metaxas, "Efficient mr image reconstruction for compressed mr imaging," *Med. Image Anal.*, vol. 15, no. 5, pp. 670–679, 2011.
- [57] M. Lustig, D. Donoho, and J. M. Pauly, "Sparse MRI: The application of compressed sensing for rapid mr imaging," *Magn. Reson. Med.*, vol. 58, no. 6, pp. 1182–1195, 2007.
- [58] C. Y. Lin and J. A. Fessler, "Efficient dynamic parallel MRI reconstruction for the low-rank plus sparse model," *IEEE Trans. Comput. Imag.*, vol. 5, no. 1, pp. 17–26, 2018.
- [59] S. Babu, S. S. Nayer, S. G. Lingala, and N. Vaswani, "Fast low rank column-wise compressive sensing for accelerated dynamic MRI," in *Proc. IEEE Int. Conf. Acoust., Speech Signal Process.*, pp. 1346–1350, IEEE, 2022.
- [60] J. Caballero, A. N. Price, D. Rueckert, and J. V. Hajnal, "Dictionary learning and time sparsity for dynamic mr data reconstruction," *IEEE Trans. Med. Imag.*, vol. 33, no. 4, pp. 979–994, 2014.